Research Article Vol. 15, No. 4 / 1 Apr 2024 / Biomedical Optics Express 2481
Biomedical Optics EXPRESS

Optical signatures of thermal damage on ex-vivo brain, lung and heart tissues using time-domain diffuse optical spectroscopy

ALESSANDRO BOSSI,[1,2,*] LEONARDO BIANCHI,[1] PAOLA SACCOMANDI,[1] AND ANTONIO PIFFERI[2]

[1]Department of Mechanical Engineering, Politecnico di Milano, via Giuseppe La Masa 1, 20156 Milan, Italy
[2]Department of Physics, Politecnico di Milano, Piazza Leonardo da Vinci 32, 20133, Milan, Italy
*alessandro.bossi@polimi.it

Abstract: Thermal therapies treat tumors by means of heat, greatly reducing pain, post-operation complications, and cost as compared to traditional methods. Yet, effective tools to avoid under- or over-treatment are mostly needed, to guide surgeons in laparoscopic interventions. In this work, we investigated the temperature-dependent optical signatures of ex-vivo calf brain, lung, and heart tissues based on the reduced scattering and absorption coefficients in the near-infrared spectral range (657 to 1107 nm). These spectra were measured by time domain diffuse optics, applying a step-like spatially homogeneous thermal treatment at 43 °C, 60 °C, and 80 °C. We found three main increases in scattering spectra, possibly due to the denaturation of collagen, myosin, and the proteins' secondary structure. After 75 °C, we found the rise of two new peaks at 770 and 830 nm in the absorption spectra due to the formation of a new chromophore, possibly related to hemoglobin or myoglobin. This research marks a significant step forward in controlling thermal therapies with diffuse optical techniques by identifying several key markers of thermal damage. This could enhance the ability to monitor and adjust treatment in real-time, promising improved outcomes in tumor therapy.

1. Introduction

Thermal therapies are a set of emerging methods [1] utilized to treat localized tumors in several organs, such as the brain [2,3], lungs [4], liver [5], and pancreas [6]. Various types of thermal therapies exist, and involve the use of diverse energy sources, including laser [7], microwave [8] and radiofrequency [9]. Despite their differences, these techniques rely on the deposition of heat in the tumor to induce tissue death, either through apoptosis or necrosis [1]. The major advantage of thermal therapies compared to current treatment methods is their minimally invasive nature. In many cases, only a small incision for catheter insertion is necessary to access the treatment site. This minimally invasive approach contrasts with traditional methods and open surgery, and offers several benefits including: i) improved patients' quality of life [10] as the procedure allows for a shorter recovery period ii) reducing complications related to surgery iii) making treatment viable for previously inoperable cancers iv) reducing operational costs as shorter post-surgery hospital care is required.

However, these minimally invasive methods also come with limitations. Notably, surgeons may find it challenging to access and inspect the treatment area, a concern not present in open-chest surgeries where visual and tactile feedback are immediately available. Ensuring the complete treatment of tumor tissue, while leaving unharmed surrounding healthy tissue, is vital in cancer treatment. Moreover, in the case of thermal therapies, it is crucial to prevent tissue carbonization, which is harmful to the body [11]. Therefore planning and real-time control of the therapy are of paramount importance [12]. To control the treatment, current strategies employ thermometry,

#517376 https://doi.org/10.1364/BOE.517376
Journal © 2024 Received 2 Jan 2024; revised 21 Feb 2024; accepted 21 Feb 2024; published 19 Mar 2024

Biomedical Optics EXPRESS

based on Magnetic Resonance Imaging [13] or on contact sensors. Fiber Bragg grating sensors (FBGs) are very promising: they are micron-sized fiber-optic cables that allow temperature measurements over multiple points along the fiber [14]. By using multiple FBGs, one can achieve a tomographic reconstruction of the temperature distribution in the treated tissue and perform a feedback mechanism to confine the ablation zone [15–17]. Although temperature is a key parameter to directly assess the amount of energy absorbed by the tissues, a main limitation is the challenge of classifying the resulting thermal damage. Along with the temperature locally reached during thermal therapies, the exposure time is also a meaningful parameter for the thermal damage determination [18]. The combined information of tissue temperature and exposure time offer an indirect estimation of tissue damage, typically derived from a first-order Arrhenius thermal damage model [19] and the Cumulative Equivalent Minutes at 43 °C (CEM43) [20]. In cancer treatment, a primary metric for thermal damage is the cells' survivability to treatment, but the direct measurements of this quantity in biological environments pose challenges. However, alternative indicators of thermal damage, such as the state of proteins and chemical composition which change during treatment, can serve as valuable proxies to evaluate thermal damage. These markers might be evaluated by measuring the reduced scattering and absorption coefficients. The reduced scattering coefficient, i.e., μ_s', offers insights into tissue microstructure [21], which is intimately linked with its protein state. On the other hand, the absorption coefficient, i.e., μ_a, reveals information about the tissue chemical composition [22].

A particularly relevant wavelength range for studying μ_a and μ_s' of biological tissues is 650 nm to 1100 nm where μ_s' is 2-3 orders of magnitude larger than μ_a. Therefore, the photons' travel through tissue is governed by the diffusion equation [23]. Within this wavelength region in tissues, the main absorbers are: hemoglobin, myoglobin, water, lipids, and collagen [24]. The measurement of μ_a and μ_s' can be performed with diffuse optical techniques [25]. Some optical methods, relying on continuous-wave techniques [26–30] or hyperspectral imaging [31], have been already investigated to describe the thermal damage in organs undergoing thermal therapies. However, these techniques present depth probing limitations and the inability to disentangle μ_a from μ_s'. In contrast, time-domain techniques, like Time-domain Diffuse Optical Spectroscopy (TD-DOS), introduce the dimension of time to provide a more accurate estimation and depth sensitivity of the optical properties [32]. The time domain approach utilizes ps-pulses of light injected in the tissue and measures the photon distribution of time of flight (DTOF). These laser pulses in tissues broaden temporally due to scattering and attenuate following the Beer-Lambert law, enabling a clear distinction between the two coefficients in the measured DTOF. Furthermore, photons detected at later times have traveled a longer path within the tissue and probed a deeper region. As a result, TD-DOS enhances the separation of photons from varying depths, providing an advantage over continuous wave (CW) techniques and provides a few cm of depth sensitivity. In previous studies of our group, TD-DOS has been used to measure the optical properties of fresh porcine skin, fat, muscle, lung, heart, brain, tendon, kidney, cortical bone [33] and porcine pancreas [34] at nominal temperature. A preliminary study using TD-DOS revealed notable changes in both μ_s' and μ_a of ex-vivo tissues undergoing radiofrequency ablation [35]. The ultimate goal is to develop a device capable of real-time monitoring of thermal damage. This requires either identification of few discrete wavelengths that better track the tissue transformation or a parallel acquisition of a broad spectral range. Further, to get access to the treated organ, it is possible either to utilize a set of multiple small-core interstitial fibers for a tomographic reconstruction of thermal damage or a single needle hosting the injection-detection fibers at null source-detection separation [36] for a more localized and less invasive modality – yet with harder constraints on the detection side

In this paper, our objective is to detail the thermal-induced alterations in μ_a and μ_s' and attempt to correlate them with known tissue chemical changes. To achieve this goal we employed a three-step thermal treatment on *ex-vivo* specimens (heart, lungs, and brain) using a thermal bath.

Biomedical Optics EXPRESS

This setup aims to achieve a stationary temperature, ensuring minimal concurrent reactions, and facilitating the isolation changes within real organs. While this approach does not replicate the dynamics of an actual therapy, following the relation between the treatment's temporal duration and temperature, detailed in the Arrhenius model's [19] of thermal damage. This allows us to measure identical reactions that occur in an actual therapy, however, with different evolution. We selected the lung, brain, and heart for analysis as they are common organs which undergo thermal treatment [2,4,37]. Moreover, due to the high variability in their microstructure and optical properties [33], these organs represent a valid model to assess the potentialities of the proposed approach.

The article is structured in three parts. In the first section, we present the measurement setup utilized to obtain the optical properties and the treatment methods used to isolate the individual reactions. In the second part we present the results obtained by the experiments for the brain, lung and heart and in the third we discuss the results and attempt to connect the findings with known chemical reactions.

2. Materials and methods

2.1. System setup and analysis of TD-DOS data

The schematic of the experimental setup is presented in Fig. 1. A homemade [33–35] broadband time-domain diffuse optical spectroscopy (TD-DOS) setup was used to measure μ_a and μ_s', of ex-vivo biological tissues. This system uses a supercontinuum laser (NKT Extreme, NKT Photonics) generating a trail of picosecond pulses with a repetition rate of 40 MHz over a large wavelength range (400 nm to 2000 nm). The radiation is sent in free beam propagation and a Pellin Broca prism is placed to disperse the radiation into the wavelength components. A lens focuses the light onto a graded index fiber with 50 μm of core and 0.2 of NA. The small dimension of the fiber and an iris limit the extracted wavelength bandwidth. Different wavelengths can be selected by rotating the Pellin Broca prism with a stepper motor. The position of the stepper motor is calibrated using a spectrometer (USB2000, Ocean Optics) to match the motor position with the output wavelength. The light is then attenuated by a circular neutral density (ND) filter placed inside a U-bracket to reach single photon statistic in detection. A couple of 1 mm core, 0.39 NA step-index fibers, set at a relative distance of 1 cm, inject and collect light to and from the sample. A silicon photomultiplier (SiPM) detects the arriving photons and the DTOF is reconstructed using a time-correlated single photon counting (TCSPC) board (SPC130, Becker and Hickl). To retrieve the spectra of μ_a and μ_s', we measured the DTOF with different probing wavelengths, from 657 nm to 1107 nm, at steps of 10 nm. Each curve is integrated for 1 s, acquiring a complete spectrum in approximately 100 s. In this experiment, the spectra were collected every 400 s. The spectral resolution of the system varies with the probing wavelength, from 3 nm at 657 nm to 10 nm at 1064 nm.

The retrieve μ_a and μ_s' from the measurements, we used a Levenberg–Marquardt optimization algorithm that compares the measured DTOF to the convolution of a theoretical model with the measured instrument response function (IRF). The model of photon migration is based on a numerical solution of the Radiative Transfer Equation using a Monte Carlo code [38]. More in detail, a GPU accelerated Monte Carlo code is used to construct a library of DTOFs for a discrete set of μ_s' values and null μ_a (white Monte Carlo). A model solution for a given set of μ_a and μ_s' values is generated by a linear interpolation of the library series corresponding to the two nearest μ_s' values, and applying the Lambert-Beer factor $exp(-\mu_a \frac{c}{n} t)$, to account for absorption, where c is the speed of light, and we assume $n = 1.4$ for the refractive index in the medium. Since μ_s' lacks fine details in the spectrum in this wavelength range, we constrained the scattering spectrum to follow the Mie power law [39,40] $\mu_s'(\lambda) = A(\frac{\lambda}{\lambda_0})^{-b}$ where A and b are free fitting parameters and we set $\lambda_0 = 657$ nm [22]. The IRF was obtained by placing the source fiber in contact with the detection fiber with a small Teflon piece in between, to excite all the modes in

Biomedical Optics EXPRESS

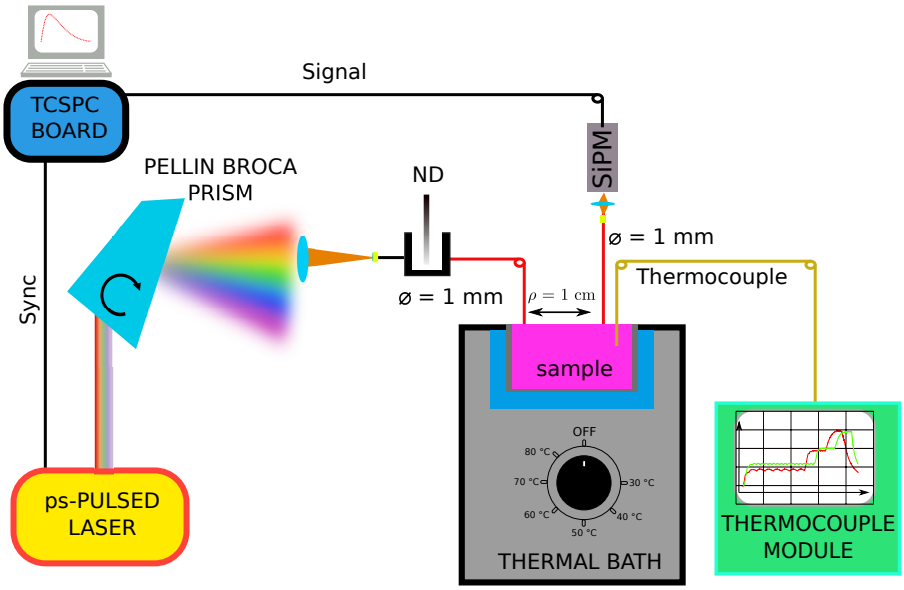

Fig. 1. Scheme of the experimental setup. Light from a picosecond-pulsed laser is directed through a Pellin-Broca prism, moved by a stepper motor, and then collected by a multimode fiber. The intensity of this light is adjusted using a neutral density (ND) filter before it illuminates a sample in a thermal bath. Light diffused from the sample is captured $\rho = 1$ cm away by a Silicon Photomultiplier (SIPM). Finally, a Time-Correlated Single Photon Counting (TCSPC) Board processes the detected photons, reconstructing a histogram for analysis.

the detection fiber. Each mode represents a different path that light can take through the fiber. The light interaction with the fiber's physical structure generates unique spatial profiles and propagation speeds thus affecting the arrival time.

For illustration purposes, Fig. 2 displays the IRF, DTOF, and fitted curve corresponding to a single wavelength. In our study, this procedure is in parallel applied to 46 curves, with the spectral constraint on μ_s' enabling the retrieval of the Mie parameters A and b.

2.2. *Tissue samples and protocol*

We aimed to measure the evolution of μ_a, μ_s', A and b coefficients during thermal treatment of three biological tissues (i.e., heart, brain and lung tissues) and study the related spectral changes. The A and b parameters contain information on the number and size of the scattering centers, respectively [21].

The measurements were performed while the biological tissues were placed in a thermal bath, to provide controlled temperature conditions. The samples were placed in a metallic cup, which is in turn immersed in water at a controlled temperature. This heating process was aimed to attain a stable temperature over time and a uniform temperature distribution across the sample. The uniform heat distribution, generates uniform changes in the sample which simplifies the reconstruction of μ_a and μ_s' by allowing the use of a semi-infinite model, while the step-like reactions simplify the spectra interpretation and the study of the optical properties evolution.

To capture the evolution of the optical properties over time, we continuously measured while we set the water bath at three different temperatures: $T_{set} = 43$ °C for approximately 12 hours (phase 1), $T_{set} = 60$ °C (phase 2) and $T_{set} = 80$ °C (phase 3) each for 4 hours. We then left the sample to cool (cooling phase) for 1 hour. The samples at the end of treatment had a temperature

Biomedical Optics EXPRESS

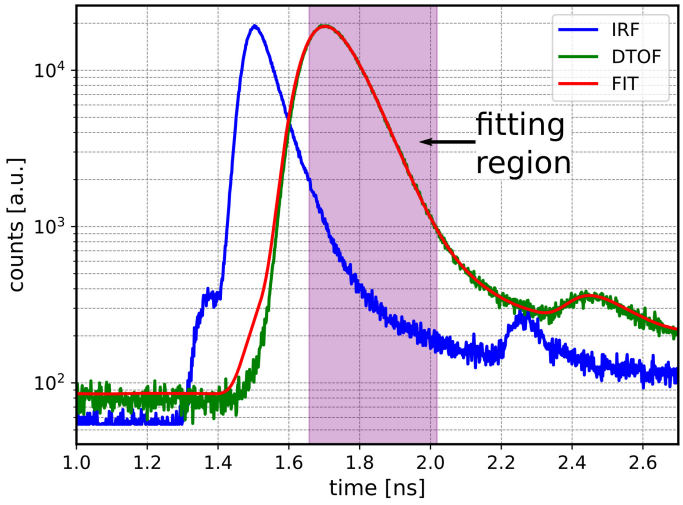

Fig. 2. Example of the fitting process for a single curve without the spectral constant used in this work. We show the Impulse response function (IRF) of the system, the distribution of time of flights (DTOF) and the fitted curve. Moreover we highlighted the fitting region employed in the procedure: from 80% of the maximum on the rising edge to 5% of the maximum on the falling edge.

of approximately 40 °C. This resulted in roughly 22 hours of measurement for each sample. Given the slow progression of the process and the slow change in the temperature, we can treat the measurements at the initial time as representing the untreated sample, which we will subsequently refer to as 'native'. These temperatures were selected to observe changes at significant treatment levels. Specifically, 43 °C is in the hyperthermia region [1] and is a typical target treatment temperature [41], 60 °C is considered the temperature at which instantaneous damage occurs and 80 °C is within the temperature range causing ablation [1]. While higher temperatures would be of interest, the current heating device cannot achieve them. Although the water was heated up to the target temperature, due to heat loss in the environment we observed the temperature inside the sample was ∼ 1-2 °C cooler than the water. Due to water evaporation, we were required to refill the water of the thermal bath, and this operation caused a momentary decrease in the temperature. After the treatment, a few samples were blended to fully expose the tissue to air. These will be referred to as 'exposed to air'. During the whole measurement process, 3 k-type thermocouples (0.1 °C accuracy, associated with a temperature monitoring module, Yokogawa FX1000) monitored the temperature inside the sample to provide an accurate reading of the condition of treatment.

Three different organ tissues were considered in this study: ex-vivo calf lung, brain and heart. The brain and heart samples were obtained from food chain supply while the lung was obtained from a local slaughterhouse. All tissues were freshly excised, stored at 4 °C before each measurement, and then allowed to reach room temperature before proceeding with the experimental protocol. For each tissue type, three different organs were involved in the measurements, thus resulting in a total of nine measurements. Before the experiments we cut the organs to fit the metallic container that was placed in the thermal bath. The samples were 4 cm thick in order to avoid boundary effects for the light propagation.

Biomedical Optics EXPRESS

3. Results

The system was validated following the MEDPHOT protocol [42] for performance assessment of diffuse optics instruments, which implies tests on accuracy, linearity, noise, stability and reproducibility, as reported in a description of the system [43] and in a multilaboratory performance assessment exercise [44]. However, to evaluate the performance and response characteristics of the system with the optical properties observed in this work that are beyond the one foreseen in the MEDPHOT protocol, we conducted experiments designed to investigate the linearity of its optical properties up to extremely high values of μ_a and μ_s'. These experiments utilized phantoms made from a mixture of Intralipid, water, and ink, following a multilaboratory study on the characterization of liquid phantoms [45]. The relation between the ink concentration and the measured μ_a is illustrated in Fig. 3 at different Intralipid concentrations. Specifically, we investigated μ_s', within the range of 5 to 35 cm^{-1}, and μ_a, within the range of 0 to 1.6 cm^{-1}. These parameters were chosen to mimic the optical properties observed in the treated tissues. We observe a good linearity between the ink concentration and the absorption coefficient, with some instabilities at very high absorption, and a fairly good independence of scattering.

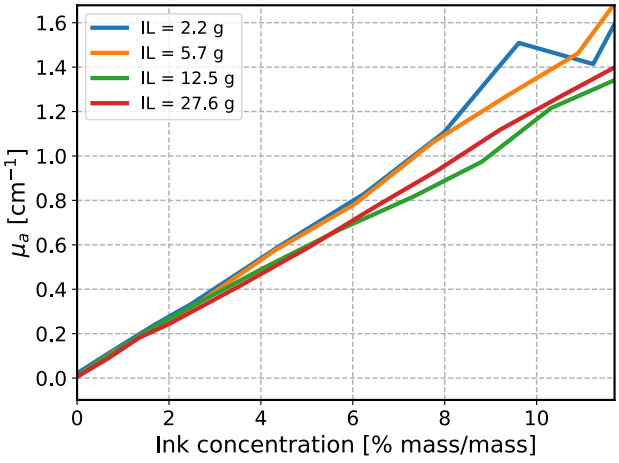

Fig. 3. Fitted absorption coefficient (μ_a) as a function of ink concentration at different Intralipid concentrations. The Intralipid concentration determines the reduced scattering coefficient (μ_s'). We can see a good linearity between the ink concentration and μ_a thus indicating a good reconstruction of the optical property in the conditions encountered in the experiment.

In the following, we present the results separately for the reduced scattering coefficient (μ_s') and the absorption coefficient (μ_a), as these parameters are fundamentally independent.

3.1. Absorption coefficient

The absorption spectra for lung, heart, and brain tissues, observed at various stages of thermal treatment, are displayed in Fig. 4. All spectra are averaged across three samples to provide an estimation of the mean and standard deviation of the optical property.

Our analysis reveals a relatively low standard deviation across all organs, allowing us to focus on the results of a single trial for simplicity. Consistent trends were observed in multiple trials for each type of organ tissue.

In Fig. 5 we show the spectra of μ_a for a single repetition emphasizing the changes happening during a thermal treatment and highlight the regions of interest. Each type of organ tissue

Biomedical Optics EXPRESS

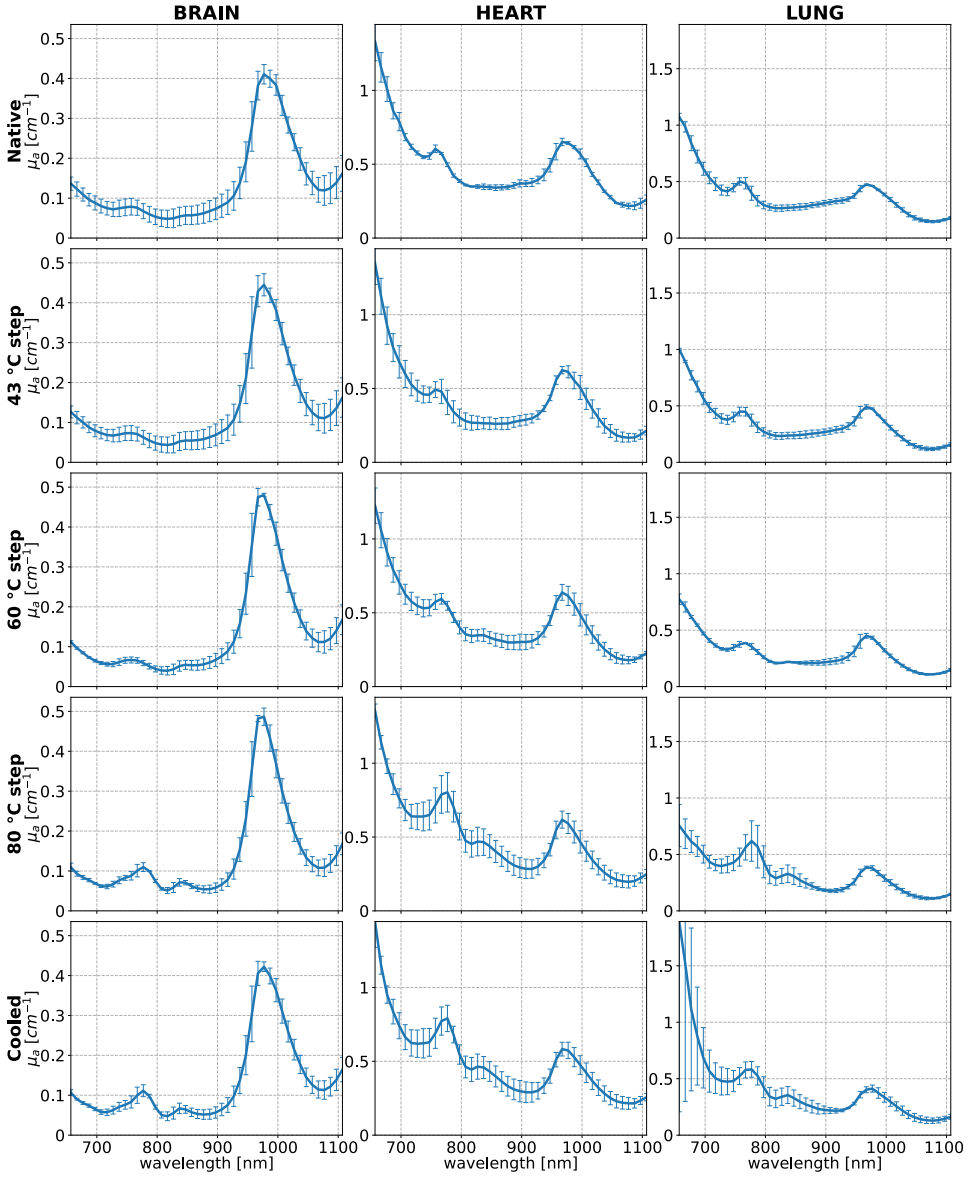

Fig. 4. Absorption spectra of brain, heart and lung at five treatment steps: sample untreated (native), after 12 h at 43 °C, after 4 h at 60 °C, after 4 h at 80 °C and after cooling. The spectra are averaged over the three repetitions of the measurements, and results are reported as mean ±standard deviation.

Biomedical Optics EXPRESS

possesses a unique absorption spectrum, however, commonalities exist. all samples consistently display a significant absorption peak at 970 nm, indicative of water's presence. Furthermore, a peak at 750 nm, corresponding to myoglobin (Mb) and hemoglobin (Hb), is observed in untreated samples. Specifically, heart and lung tissues exhibit increased absorption (μ_a) below 950 nm, attributed to a high concentration in hemoglobin and myoglobin.

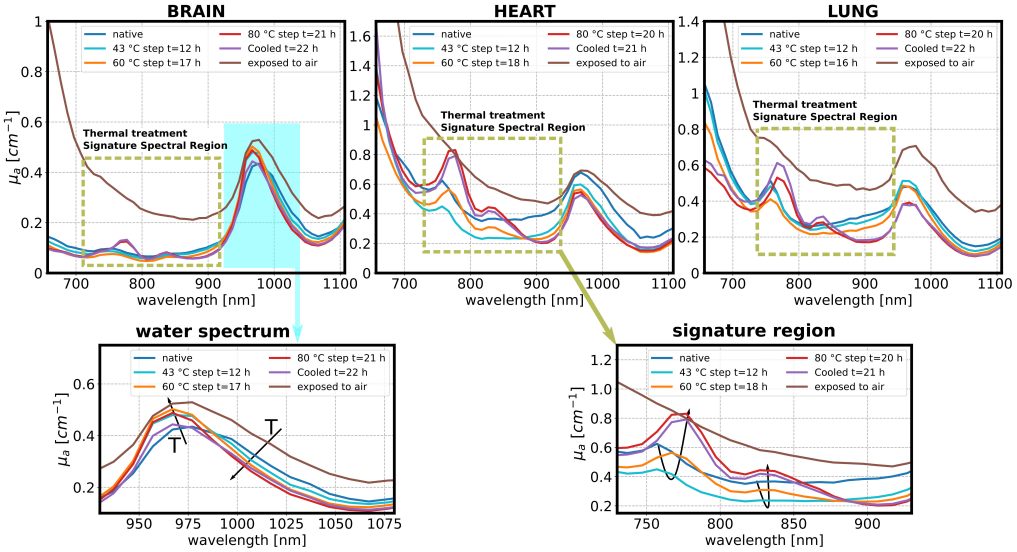

Fig. 5. Absorption spectra for one repetition for brain, heart and lung at five treatment steps: sample untreated (native), after 12 h at 43 °C, after 4 h at 60 °C, after 4 h at 80 °C, after cooling, and exposed to air. The sample exposed to air was blended and then remeasured after a few minutes. We highlight under the plot two regions: the region of the water peak that experiences a blueshift with the temperature and the region that we defined as the "thermal treatment signature region".

During Phase 1, targeting a temperature of 43 °C, a fast reduction in μ_a is noted in lung tissues, minimal changes in the brain tissues and a reduction over the whole phase in two out of three heart samples. The spectral profiles largely remain unchanged. In Phase 2, aiming for a temperature of 60 °C, there are some minimal sample dependent changes in the amplitude of μ_a over the whole spectra. A further reduction in the lung is noted. This phase also reveals subtle spectral features, such as a slight peak at 830 nm in heart and lung tissues, a dip at around 910 nm in heart tissues, and a diminished 750 nm peak. These changes become more apparent in Phase 3. Phase 3, conducted at 80 °C, showcases significant spectral alterations in all samples. New peaks at 770 nm and 830 nm become evident, alongside a distinct dip at approximately 910 nm in both lung and heart tissues. During cooling no significant changes are reported. Following the treatment, selected tissues were blended and subsequently exposed to air before being remeasured. This process resulted in the disappearance of the peaks at 770 nm and 830 nm, alongside a significant increase in the spectral region below 850 nm, when compared to the spectra of the cooled tissues. A high increase was noted in the brain tissue.

Throughout the thermal treatment process, a blue shift in the 970 nm water peak is observed and reverts to its initial state during the cooling phase.

3.2. *Reduced scattering coefficient*

The scattering spectra for lung, heart, and brain tissues, observed at various stages of thermal treatment, are displayed in Fig. 6. All spectra are averaged across three samples to provide an

Biomedical Optics EXPRESS

estimation of the mean and standard deviation of the optical properties. The scattering spectra do not exhibit specific spectral features as we applied the Mie Power law constraints and derived the parameters A and b. The variability observed in the evolution of μ_s' likely stems from factors such as differences among specimens, variations in measurement locations, storage conditions, and minor fluctuations in treatment temperatures.

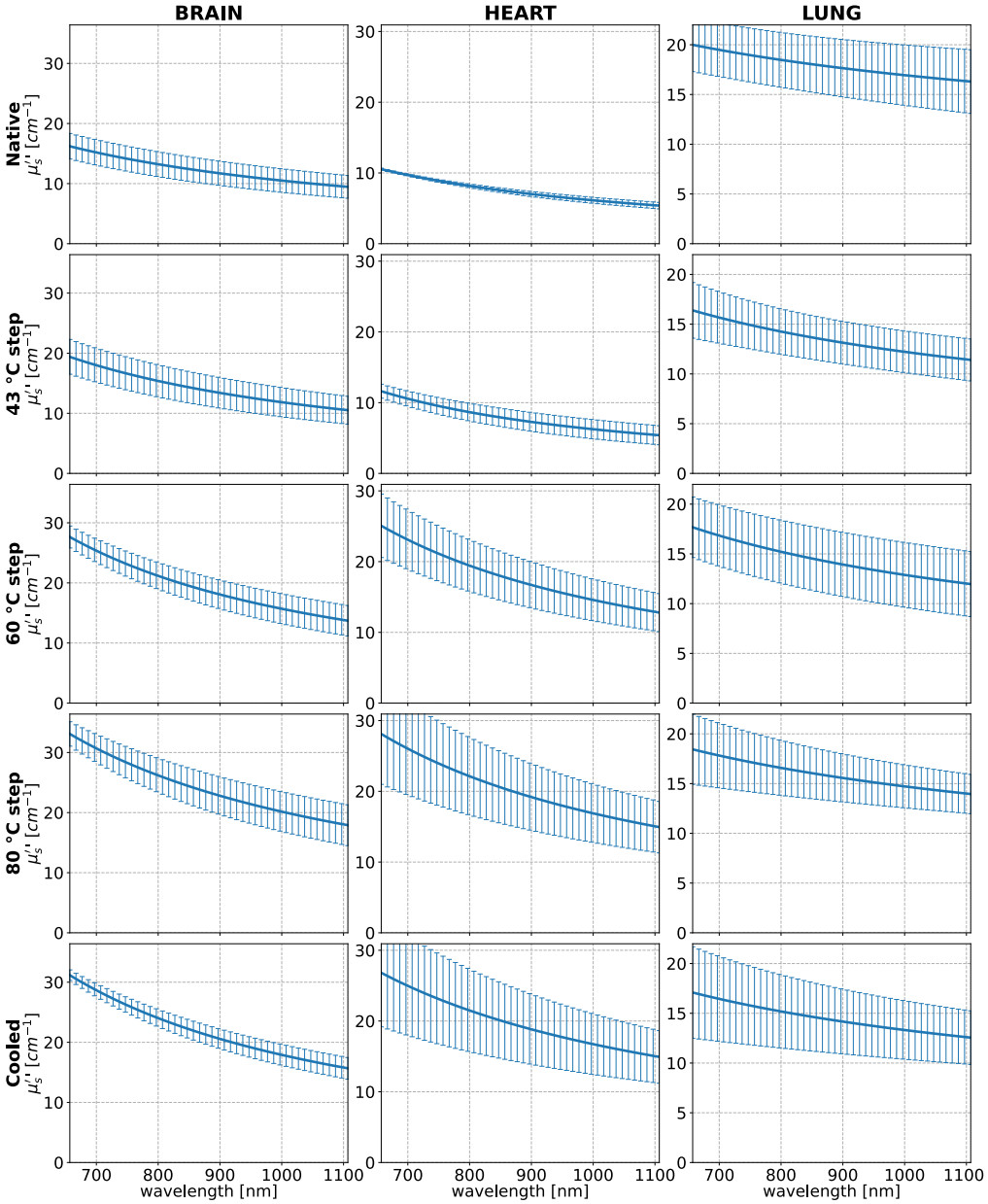

Fig. 6. Reduced scattering coefficient spectra of brain, heart and lung at five treatment steps: sample untreated (native), after 12 h at 43 °C, after 4 h at 60 °C, after 4 h at 80 °C and after cooling. The spectra are averaged over the three repetitions of the measurements, and results are reported as mean ±standard deviation.

Biomedical Optics EXPRESS

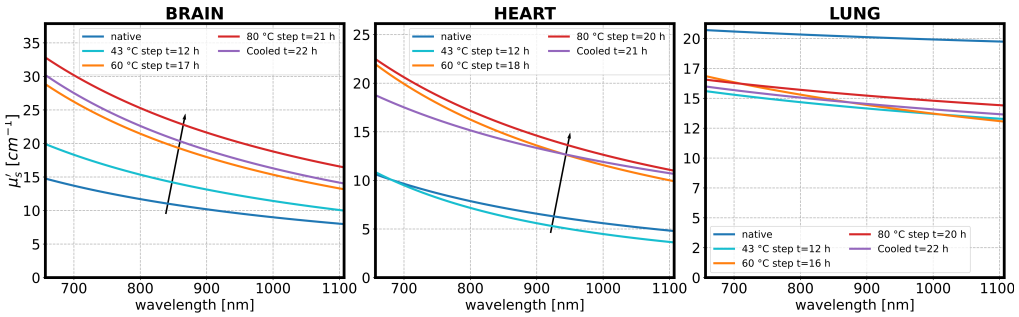

Fig. 7. Reduced scattering (μ'_s) spectra for one repetition for brain, heart and lung at five treatment steps: sample untreated (native), after 12 h at 43 °C, after 4 h at 60 °C , after 4 h at 80 °C and after cooling.

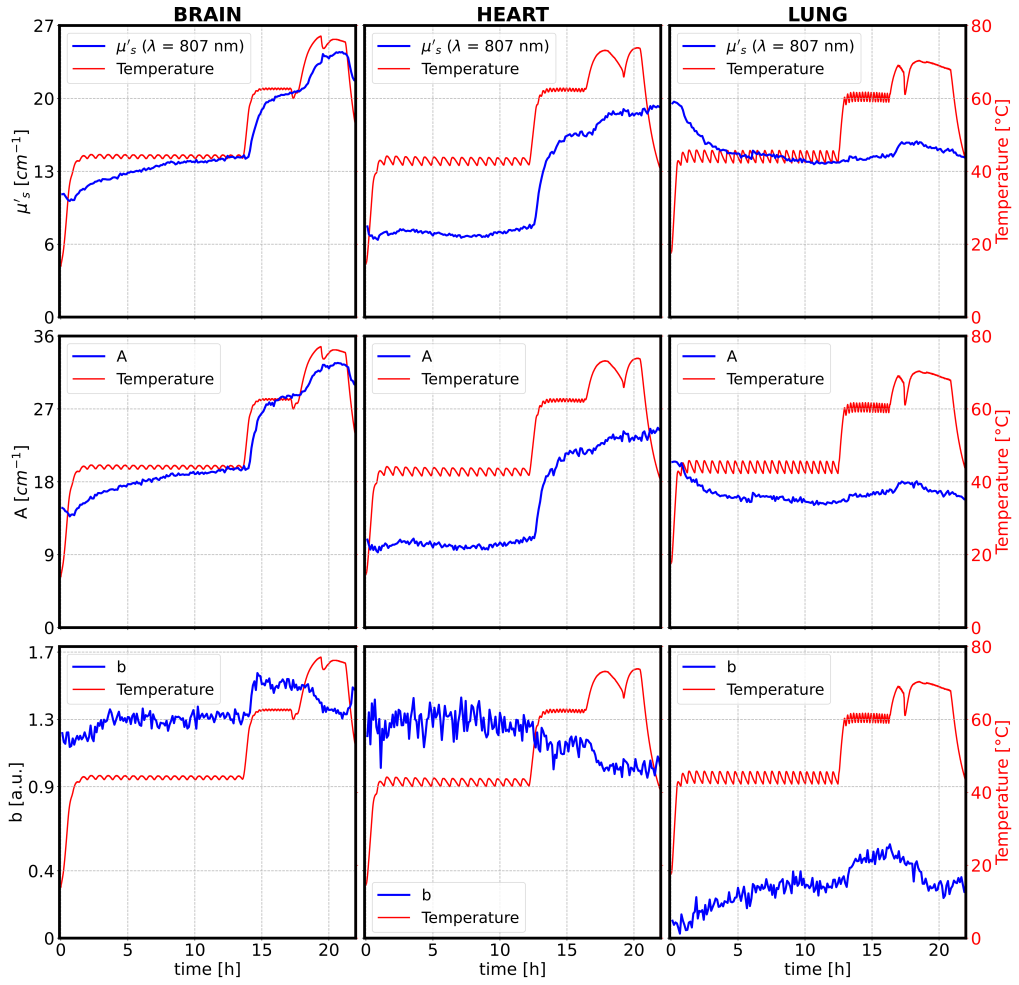

Fig. 8. Evolution of the reduced scattering coefficient (μ'_s, λ = 807 nm) (top), A (center) and b (bottom), for brain, lung and heart and the temperature evolution inside the sample during the treatment for one repetition of the experiment.

Biomedical Optics EXPRESS

Also for scattering, we present a single sample evolution to better appreciate relative thermal changes, as reported in Fig. 7.

Throughout the study, we identified seven principal characteristics in the evolution of μ_s' across different phases: i) a slight but notable increase in μ_s' at the onset of treatment (Phase 1, T_{set} = 43 °C) in some heart tissue samples and brain; ii) a pronounced increase during Phase 2 (T_{set} = 60°C) in heart and brain tissues; iii) an additional increase in Phase 3 (T_{set} = 80°C) in heart and brain tissues; iv) a decrease in μ_s' in the brain and lung in the first hour of treatment; v) a horizontal asymptotic trend in μ_s' evolution after several hours at each treatment phase; vi) more limited μ_s' alterations in lung tissue throughout the treatment; vii) a minor decrease in μ_s' during cooling in the brain and no changes in the lung and heart.

To study more continuously the temporal changes of the scattering properties, Fig. 8 displays the temporal evolution of μ_s' at 837 nm (top row), and the *spectral* parameters A (center row) and b (bottom row). For reference, the measured temperature T is displayed in all graphs. The parameter A exhibits a close alignment with the observed evolution in μ_s'. There is a higher degree of variability observed in the repetitions of b. However, we can identify general trends: in the brain, b demonstrates an increase during phase 1 and a decrease in phase 3. In the heart, b shows minimal changes. Meanwhile, in the lung, there is an observed increase in phase 1 and a decrease in phase 3.

4. Discussion

By exploring the linearity of the response of the absorption coefficient with the ink concentration we can claim that the results obtained well represent the optical properties. Still, our study's precision is constrained by the short distance between the source and detector (1 cm), a necessity due to the strong light attenuation caused by extremely high scattering (μ_s', up to 40 cm^{-1}) and absorption coefficients (μ_a, up to 1.6 cm^{-1}) observed in our experiments. We can focus independently on μ_a or on μ_s' in our analysis, as they are governed by two different physical processes. μ_a is linked with the chemistry of the tissue, while μ_s' is related to changes of the refractive index, and therefore to alterations in the microstructure of the tissue. From μ_s' we can probe the state of tissue proteins, the arrangement of fibrils, the organization of fibers, and the morphology of cells and organelles [39].

4.1. Absorption coefficient

Each organ tissue exhibits a unique absorption spectrum, a phenomenon attributable to the varying concentrations of chemical compounds present. The absorption spectra of different tissues demonstrate shared characteristics and trends when subjected to thermal treatment. This commonality stems from the Beer-Lambert law, which states that the absorption spectrum derives from:

$$\mu_a(\lambda) = \sum_i c_i \epsilon(\lambda) \tag{1}$$

where c_i is the molar concentration and $\epsilon(\lambda)$ is the molar attenuation coefficient of the i^{th} chromophore. In biological tissues the main chromophores are: deoxygenated hemoglobin (Hb), oxygenated hemoglobin (HbO_2), deoxymyoglobin (Mb), oxygenated myoglobin (MbO_2), collagen, lipids, water, [22] methemoglobin (MetHb), and metmyoglobin (MetMb). Notably for lung and heart, the absorption coefficient (μ_a) is high below 950 nm due to the abundant presence of Mb, MbO_2, Hb, and HbO_2, all of which exhibit high absorption at shorter wavelengths [46]. We assume that the heart and lungs contain a considerable amount of the oxygenated forms of these compounds, as evidenced by the high absorption values around 900 nm, aligning with the absorption spectra of HbO_2 and MbO_2 [46]. Furthermore, we assume in the heart the presence of myoglobin, reflecting its muscular makeup, whereas hemoglobin is assumed present in the lungs

Biomedical Optics EXPRESS

and the brain, given their vascular nature. We highlight that hemoglobin and myoglobin within blood and muscles exist mainly three states: oxygenated, deoxygenated, and a non-reversibly binding form known as methemoglobin or metmyoglobin, the latter being prevalent in the final phases of treatment [47]. The met state is the commonly known denatured state of heme proteins induced by elevated temperatures.

During the whole treatment we observe the blueshift of the 970 nm peak, which is due to the weakening of hydrogen bonds with increasing temperature [48].

At 43 °C and 60 °C, the spectral profiles largely remain unchanged, suggesting the absence of notable chemical reactions. The observed decrease in μ_a across the spectrum can be attributed to: i) reconstruction errors stem from inaccuracies in the semi-infinite model; ii) fitting errors due to an interaction between μ_a and μ_s'; iii) possible temperature mediated reactions that we have not identified; iv) temperature alterations of the extinction coefficient of some chromophores, as already reported for water; iv) tiny detachment of the sample from the probe that adds a temporal shift in the DTOF.

At 80 °C we interpret the development of the 770 nm and 830 nm peaks to be caused by the denaturation of the deoxygenated state of blood proteins, leading to the formation of new chromophores. We speculated that these new chromophores are related to myoglobin and hemoglobin, although distinct from the met state, as suggested by differences in spectral shape from the one found in literature [46] of methemoglobin. We point our attention to a different form of the heme protein that is meta-stable and highly reactive with oxygen because: i) the intensity seems correlated with the original 750 nm peak of Hb or Mb; ii) it was linked with hemoglobin in a previous article [35]; iii) lipids do not change their chemical structure in this temperature range; iv) proteins change their secondary structure [49] in this temperature range but this should cause only minor wavelength shifts; v) water presents a peak at 760 nm and 840 nm but it is much weaker compared to the ones measured; vi) we assume the absence of carbon monoxide in the tissue [50], so we exclude carboxyhemoglobin, vii) Ref. [50] notes the formation of NO-Mb in the presence of nitrous acid but we tend to exclude its presence; viii) Maillard reactions [51] are present at higher temperatures and are not influenced by oxygen.

We demonstrate the high reactivity with oxygen by blending one sample per organ tissue and exposing it to air for a few minutes post-measurement. We observed that the 770 nm and 830 nm peaks disappear as shown in Fig. 5, and similarities with the Met state in blood were observed. This leads us to put forward the hypothesis that the Met state forms only in the presence of oxygen, while a meta-stable state develops in its absence. Our experiments indicate that this particular chemical structure vanishes in the presence of oxygen. Consequently, for realistic ablation procedures, it is imperative to consider this dynamic as in-vivo treatments are characterized by an oxygen-rich environment, potentially leading to the formation of the Met form as opposed to the one observed in this work. This explanation agrees with measurements performed in CW and hyperspectral techniques [28,31,52,53], where they do not report the presence of those peaks, as the probing depth is limited only to a few mm and the sample is in contact with the air.

To substantiate or refute this claim, it is indispensable to employ more chemically sensitive techniques. Specifically, investigating the novel chemical structure of the heme protein would benefit from employing methods such as Raman spectroscopy [54]. Particularly diffuse Raman spectroscopy [55,56] could in principle be able to probe inside a media while maintaining the high specificity of Raman spectroscopy and probe the same depth regions as the one observed in this study. Moreover, nuclear magnetic resonance, and consultation with an anatomic pathologist can be valuable. Additionally, a noticeable reduction of μ_a at 900 nm, observed in the heart and lung, is likely associated with the denaturation of the oxygenated state into the met form and the emergence of the new chromophore discussed earlier. During cooling, no spectral changes were observed, indicating no chemical changes happening.

Biomedical Optics EXPRESS

4.2. Reduced scattering coefficient

The change in the parameter A relates with the change in the number of the scattering centers, and follows closely the evolution of μ_s'. Interestingly, the parameter b shows no significant change from its initial value in most tissues, suggesting negligible changes in the size of scattering centers. However, lung tissue exhibits a notable exception, with an initial decrease in b followed by an increase. This pattern suggests alterations in the size of alveoli scattering centers, possibly due to thermal effects on lung tissue microstructure.

Our results show an increase in μ_s' across tissues with the treatment, in agreement with other studies [26,35] in brain and heart tissues, with lung tissues exhibiting minimal variations. This trend reinforces the complex yet systematic nature of tissue responses to thermal treatments, offering insights into the underlying mechanisms of thermal effects on biological tissues.

The observed features of μ_s' and A can be associated with denaturation processes [39], which are crucial factors in the cellular breakdown and the disintegration of muscle fibers. Our analysis has primarily focused on collagen, myosin, and lipids, as these molecules are the principal components of organ matrices. However, our interpretation remains speculative, as our methodology does not allow the differentiation of signals originating from different scattering centers. The explanation that we present draws upon the composition of the organs and a comprehensive review of existing literature on the denaturation processes at different temperatures. We have made several observations: i) for the increase in μ_s' of brain and some heart tissues, during treatment at 43 °C, Ref. [57] suggests that the denaturation of monomeric collagen happens even at body temperature. We associate this result with the analysis of ex-vivo tissues. It is vital to acknowledge this phenomenon as it could underscore the distinctions between ex-vivo and in-vivo measurements. In addition, the increasing scattering could be attributed to the processes that occur post-mortem, and understanding these processes can elucidate any disparities between our measurements and the reactions taking place during an in-vivo treatment. ii) The increase at phase 2 (T_{set} = 60 °C) can be associated with triple-helix denaturation of collagen for brain and lung tissues [58] and myosin denaturation for the heart [28,59]. iii) The increase at phase 3 (T_{set} = 80 °C) is likely related to the denaturation of the secondary structure of proteins [49,60]. iv) The small decrease in μ_s' of the brain in the first hour can be linked to lipid melting due to the low melting temperature of lipids [61]. v) The differences noted in the results for the lung compared to the one of the heart and brain, we believe, are caused by the unique alveolar structure. Given the alveoli's significant role in the lung's microstructure, thermal damage is likely to induce different changes in μ_s' in the lung compared to the heart and brain. vi) Considering the horizontal asymptotic behavior observed where a change in the scattering was measured, we can assume that at each step we are measuring different reactions, as the reaction dynamics is governed by a first-order Arrhenius model [19,62] and at the end of the step there was no longer any undamaged tissue to react.

According to the Arrhenius model, the extent of damage – in this context, represented by changes in μ_s' – should follow the relative damage level $P = 1 - \exp(-\Omega)$, where Ω is the damage parameter [19] and is equal to:

$$\Omega(t) = \int_0^t A \exp(-\frac{E_a}{RT})dt \tag{2}$$

Where A [s^{-1}] is the 'frequency factor' (not to be confused with the scattering A parameter) and E_a [J/mol] is the 'Activation Energy'. $\Omega(t)$ has a monotonic increase, and the relative damage level explains the horizontal asymptotic behavior measured. This model highlights the relationship between thermal damage and the two critical factors: time and temperature. It illustrates that a reaction can indeed proceed given sufficient time at any temperature. Additionally, it reveals that our method of slow treatment at a lower temperature compared to typical clinical treatments is, in principle, capable of estimating the dynamics of optical property evolution across various treatment temperatures. This insight suggests that while our treatment conditions may differ in

Biomedical Optics EXPRESS

intensity, they still offer a valuable framework for understanding how optical properties evolve in response to thermal exposure.

4.3. Limitations and possible improvements

The main aim of this work is to measure, describe and interpret the change in the optical properties of heart, lung and brain tissues during a thermal treatment, and to try to correlate them with the reactions occurring within an organ tissue at specific temperatures. To accomplish our aim, we proceeded with some simplifications which left space for further improvements. It is also pertinent to highlight the limitation of our instrumentation, which cannot measure wavelengths below 657 nm in tissues rich in hemoglobin and myoglobin due to elevated μ_a and μ_s', leading to photon detection falling below the noise threshold. Due to the high μ_a, in parts of the spectrum the distribution of time of flights measured and the impulse response of the system may not be sufficiently separated in time to provide a precise estimation of μ_a and μ_s'. Other inaccuracies could be caused by the model geometry as we assumed a semi-infinite model since it simplified the interpretation of the result, even though this assumption may not capture the complete nuances of changes in the optical properties at different depths. The measured depth is linked to the time of arrival of photons and μ_s' as elaborated in ref. [32]. This implies that by changing the values of μ_s' and μ_a the distribution of time of flight is modified and therefore the probed depth in different repetitions is subject to variation, as the scattering changes significantly. The probed depth depends on the temporal region fitted in the distribution of time of flights. In our case, the average maximum photon depth at low values of reduced scattering and absorption ($\mu_s' = 5$ cm^{-1} and $\mu_a = 0$ cm^{-1}) is around 8 mm while at high values ($\mu_s' = 30$ cm^{-1} and $\mu_a = 0.8$ cm^{-1}) is around 4 mm.

All the measurements were performed in ex-vivo animal tissues, towards the extension of the main results in-vivo applications. However, in the case of in-vivo treatments, multiple factors come into play simultaneously, including the presence of blood which can significantly alter the absorption profile. The alteration must be considered for the concentrations of oxygenated and deoxygenated forms of the heme protein. Furthermore, the diversity within organ tissues and the location of measurement, which has not been explored in this study, is crucial for developing comprehensive therapeutic strategies. Future developments of this study would enhance the accuracy of the reported results. Indeed, working at a higher source detection distance, with a higher power laser, could unlock results with higher accuracy and allow for finer interpretations of the result, in particular b that holds valuable information on the scattering center size, that in this work we are unable to properly interpret due to the variability inter-organ and intrinsic noise. Regarding the initial phase of denaturation, the deployment of scanning calorimetry would allow the acquisition of additional information on activation energies. Lastly, the histological interpretation of the cellular alterations occurring in the biological tissues at these temperatures would foster the use of the optical properties changes as a thermal-damage monitoring tool for thermal therapies of tumors. The future perspective of this work is to perform optical-properties based thermal outcome monitoring in tumor-bearing models undergoing thermal therapy.

5. Conclusion

In this work, we presented several key markers of thermal treatment in μ_a and μ_s' spectra, detected using TD-DOS, which could be relevant for the identification and classification of thermal damage in biological tissues. From a literature overview, we attempted to link observed changes in μ_s' to various reactions of proteins, in particular myosin, collagen and protein secondary structure. Moreover, we found substantial changes for μ_a over 75 °C that were not previously explained in literature. We claim that the changes are caused by a previously unreported state of methemoglobin originating from deoxyhemoglobin which readily reacts into methemoglobin once exposed to air. By providing the complete spectra, from 657 to 1107 nm, of μ_a and μ_s' as a

Biomedical Optics EXPRESS

function of the thermal treatment, this work presents insightful spectral features that could be used to grade the thermal damage and optimize existing treatment modalities from the assessment of the changes in tissue optical properties.

Funding. Ministero dell'Università e della Ricerca (D2B8D520); Fondazione Cariplo (2017-2075).

Acknowledgement. The authors acknowledge financial support by the European Union's NextGenerationEU Programme with the I-PHOQS Infrastructure [IR0000016, ID D2B8D520, CUP B53C22001750006].

This work was also funded by Fondazione Cariplo (Grant No. 2017-2075).

The authors acknowledge the help of Prof. Maurizio Masi and Filippo Rossi.

We thank Dr. Andrea Farina for providing the Montecarlo libraries used in this work.

The authors wish to thank ZaroCarni and Dr. Parini for providing some of the samples used in the work.

Disclosures. The authors declare no potential conflicts of interest.

Data Availability. According to the open data policies of the Physics department of Politecnico di Milano, all data underlying the results presented in this manuscript is publicly available on Zenodo [63] under CC-BY license.

References

1. H. P. Kok, E. N. Cressman, W. Ceelen, *et al.*, "Heating technology for malignant tumors: a review," Int. J. Hyperthermia **37**(1), 711–741 (2020).
2. C. Chen, I. Lee, C. Tatsui, *et al.*, "Laser interstitial thermotherapy (LITT) for the treatment of tumors of the brain and spine: a brief review," J. Neuro-Oncol. **151**(3), 429–442 (2021).
3. L. K. Swartz, K. G. Holste, M. M. Kim, *et al.*, "Outcomes in patients treated with laser interstitial thermal therapy for primary brain cancer and brain metastases," Oncologist **24**(12), e1467–e1470 (2019).
4. J. A. Brookes, W. R. Lees, and S. G. Bown, "Interstitial laser photocoagulation for the treatment of lung cancer," Am. J. Roentgenol. **168**(2), 357–358 (1997).
5. F. Izzo, V. Granata, R. Grassi, *et al.*, "Radiofrequency ablation and microwave ablation in liver tumors: an update," Oncologist **24**(10), e990–e1005 (2019).
6. P. Saccomandi, A. Lapergola, F. Longo, *et al.*, "Thermal ablation of pancreatic cancer: A systematic literature review of clinical practice and pre-clinical studies," Int. J. Hyperthermia **35**(1), 398–418 (2018).
7. C. M. Pacella, G. Bizzarri, G. Francica, *et al.*, "Percutaneous laser ablation in the treatment of hepatocellular carcinoma with small tumors: Analysis of factors affecting the achievement of tumor necrosis," J. Vasc. Interv. Radiol. **16**(11), 1447–1457 (2005).
8. M. G. Lubner, C. L. Brace, J. L. Hinshaw, *et al.*, "Microwave tumor ablation: Mechanism of action, clinical results, and devices," J. Vasc. Interv. Radiol. **21**(8), S192–S203 (2010).
9. R. Tateishi, S. Shiina, T. Teratani, *et al.*, "Percutaneous radiofrequency ablation for hepatocellular carcinoma: An analysis of 1000 cases," Cancer **103**(6), 1201–1209 (2005).
10. F. A. Khan, S. S. Akhtar, and M. K. Sheikh, "Cancer treatment - Objectives and quality of life issues," Malaysian Journal of Medical Sciences **12**(1), 3–5 (2005).
11. D. Silva, M. Sharma, and G. H. Barnett, "Laser ablation vs open resection for deep-seated tumors: evidence for laser ablation," Neurosurgery **63**(Supplement 1), 15–26 (2016).
12. P. Namakshenas, F. M. Di Matteo, L. Bianchi, *et al.*, "Optimization of laser dosimetry based on patient-specific anatomical models for the ablation of pancreatic ductal adenocarcinoma tumor," Sci. Rep. **13**(1), 11053 (2023).
13. M. De Landro, C. Giraudeau, J. Verde, *et al.*, "Characterization of susceptibility artifacts in magnetic resonance thermometry images during laser interstitial thermal therapy: dimension analysis and temperature error estimation," Phys. Med. Biol. **68**(8), 085022 (2023).
14. F. Morra, M. De Landro, S. Korganbayev, *et al.*, "Spatially resolved thermometry during laser ablation in tissues: Distributed and quasi-distributed fiber optic-based sensing," Opt. Fiber Technol. **58**, 102295 (2020).
15. L. Bianchi, S. Korganbayev, A. Orrico, *et al.*, "Quasi-distributed fiber optic sensor-based control system for interstitial laser ablation of tissue: theoretical and experimental investigations," Biomed. Opt. Express **12**(5), 2841 (2021).
16. S. Korganbayev, A. Orrico, L. Bianchi, *et al.*, "PID controlling approach based on FBG array measurements for laser ablation of pancreatic tissues," IEEE Trans. Instrum. Meas. **70**, 1–9 (2021).
17. P. Namakshenas, L. Bianchi, and P. Saccomandi, "Fiber Bragg grating sensors-based assessment of laser ablation on pancreas at 808 and 1064 nm using a diffusing applicator: experimental and numerical study," IEEE Sens. J. **23**(16), 18267–18275 (2023).
18. M. W. Dewhirst, B. L. Viglianti, M. Lora-Michiels, *et al.*, "Basic principles of thermal dosimetry and thermal thresholds for tissue damage from hyperthermia," Int. J. Hyperthermia **19**(3), 267–294 (2003).
19. J. Pearce, "Mathematical models of laser-induced tissue thermal damage," Int. J. Hyperthermia **27**(8), 741–750 (2011).
20. S. A. Sapareto and W. C. Dewey, "Thermal dose determination in cancer therapy," Int. J. Radiat. Oncol. Biol. Phys. **10**(6), 787–800 (1984).
21. A. M. K. Nilsson, C. Sturesson, D. L. Liu, *et al.*, "Changes in spectral shape of tissue optical properties in conjunction with laser-induced thermotherapy," Appl. Opt. **37**(7), 1256 (1998).

Biomedical Optics EXPRESS

22. C. D'Andrea, L. Spinelli, A. Bassi, *et al.*, "Time-resolved spectrally constrained method for the quantification of chromophore concentrations and scattering parameters in diffusing media," Opt. Express **14**(5), 1888 (2006).
23. S. J. Madsen, B. C. Wilson, M. S. Patterson, *et al.*, "Experimental tests of a simple diffusion model for the estimation of scattering and absorption coefficients of turbid media from time-resolved diffuse reflectance measurements," Appl. Opt. **31**(18), 3509–3517 (1992).
24. A. Pifferi, A. Farina, A. Torricelli, *et al.*, "Review: Time-domain broadband near infrared spectroscopy of the female breast: A focused review from basic principles to future perspectives," J. Near Infrared Spectrosc. **20**(1), 223–235 (2012).
25. S. L. Jacques and B. W. Pogue, "Tutorial on diffuse light transport," J. Biomed. Opt. **13**(4), 041302 (2008).
26. V. K. Nagarajan, V. R. Gogineni, S. B. White, *et al.*, "Real time evaluation of tissue optical properties during thermal ablation of ex vivo liver tissues," Int. J. Hyperthermia **35**(1), 176–182 (2018).
27. V. K. Nagarajan, J. M. Ward, and B. Yu, "Association of liver tissue optical properties and thermal damage," Lasers Surg. Med. **52**(8), 779–787 (2020).
28. J. Xia, A. Weaver, D. E. Gerrard, *et al.*, "Heating induced optical property changes in beef muscle," J. Food Eng. **84**(1), 75–81 (2008).
29. W. C. Lin, C. Buttermere, and A. Mahadevan-Jansen, "Effect of thermal damage on the in vitro optical and fluorescence characteristics of liver tissues," IEEE J. Select. Topics Quantum Electron. **9**(2), 162–170 (2003).
30. J. P. Ritz, A. Roggan, C. T. Germer, *et al.*, "Continuous changes in the optical properties of liver tissue during laser-induced interstitial thermotherapy," Lasers Surg. Med. **28**(4), 307–312 (2001).
31. M. De Landro, I. Espíritu García-Molina, M. Barberio, *et al.*, "Hyperspectral imagery for assessing laser-induced thermal state change in liver," Sensors **21**(2), 643 (2021).
32. F. Martelli, T. Binzoni, A. Pifferi, *et al.*, "There's plenty of light at the bottom: Statistics of photon penetration depth in random media," Sci. Rep. **6**(1), 27057 (2016).
33. S. Mosca, P. Lanka, N. Stone, *et al.*, "Optical characterization of porcine tissues from various organs in the 650–1100 nm range using time-domain diffuse spectroscopy," Biomed. Opt. Express **11**(3), 1697 (2020).
34. P. Lanka, L. Bianchi, A. Farina, *et al.*, "Estimation of porcine pancreas optical properties in the 600–1100 nm wavelength range for light-based therapies," Sci. Rep. **12**(1), 14300 (2022).
35. P. Lanka, K. J. Francis, H. Kruit, *et al.*, "Optical signatures of radiofrequency ablation in biological tissues," Sci. Rep. **11**(1), 1 (2021).
36. V. Damagatla, P. Lanka, A. Brodu, *et al.*, "Interstitial null-distance time-domain diffuse optical spectroscopy using a superconducting nanowire detector," J. Biomed. Opt. **28**(12), 121202 (2023).
37. M. R. MacDonald, D. T. Connelly, N. M. Hawkins, *et al.*, "Radiofrequency ablation for persistent atrial fibrillation in patients with advanced heart failure and severe left ventricular systolic dysfunction: a randomised controlled trial," Heart **97**(9), 740–747 (2011).
38. A. Pifferi, P. Taroni, G. Valentini, *et al.*, "Real-time method for fitting time-resolved reflectance and transmittance measurements with a monte carlo model," Appl. Opt. **37**(13), 2774–2780 (1998).
39. J. R. Mourant, J. P. Freyer, A. H. Hielscher, *et al.*, "Mechanisms of light scattering from biological cells relevant to noninvasive optical-tissue diagnostics," Appl. Opt. **37**(16), 3586–3593 (1998).
40. X. Wang, B. W. Pogue, S. Jiang, *et al.*, "Approximation of Mie scattering parameters in near-infrared tomography of normal breast tissue in vivo," J. Biomed. Opt. **10**(5), 051704 (2005).
41. J. Crezee, N. A. Franken, and A. L. Oei, "Hyperthermia-based anti-cancer treatments," Cancers **13**(6), 1240 (2021).
42. A. Pifferi, A. Torricelli, A. Bassi, *et al.*, "Performance assessment of photon migration instruments: the medphot protocol," Appl. Opt. **44**(11), 2104–2114 (2005).
43. S. K. V. Sekar, A. Dalla Mora, I. Bargigia, *et al.*, "Broadband (600–1350 nm) time-resolved diffuse optical spectrometer for clinical use," IEEE J. Sel. Top. Quantum Electron. **22**(3), 406–414 (2016).
44. P. Lanka, L. Yang, D. Orive-Miguel, *et al.*, "Multi-laboratory performance assessment of diffuse optics instruments: the bitmap exercise," J. Biomed. Opt. **27**(07), 074716 (2022).
45. L. Spinelli, M. Botwicz, N. Zolek, *et al.*, "Determination of reference values for optical properties of liquid phantoms based on intralipid and india ink," Biomed. Opt. Express **5**(7), 2037–2053 (2014).
46. M. Van Gastel, S. Stuijk, and G. De Haan, "Camera-based pulse-oximetry - validated risks and opportunities from theoretical analysis," Biomed. Opt. Express **9**(1), 102 (2018).
47. L. L. Randeberg, A. J. Daae Hagen, and L. O. Svaasand, "Optical properties of human blood as a function of temperature," Lasers in Surgery: Advanced Characterization, Therapeutics, and Systems XII **4609**, 20–28 (2002).
48. S. H. Chung, A. E. Cerussi, S. I. Merritt, *et al.*, "Non-invasive tissue temperature measurements based on quantitative diffuse optical spectroscopy (DOS) of water," Phys. Med. Biol. **55**(13), 3753–3765 (2010).
49. R. Dong, X. Yan, X. Pang, *et al.*, "Temperature-dependent Raman spectra of collagen and DNA," Spectrochimica Acta - Part A: Mol. Biomol. Spectrosc. **60**(3), 557–561 (2004).
50. S. P. Suman and P. Joseph, "Myoglobin chemistry and meat color," Annu. Rev. Food Sci. Technol. **4**(1), 79–99 (2013).
51. P. Nath, N. Pandey, M. Samota, *et al.*, "Browning Reactions in Foods," *Advances in Food Chemistry: Food Components, Processing and Preservation* (Springer, 2022), pp. 117–159.
52. E. Tanis, J. W. Spliethoff, D. J. Evers, *et al.*, "Real-time in vivo assessment of radiofrequency ablation of human colorectal liver metastases using diffuse reflectance spectroscopy," Eur. J. Surg. Oncol. **42**(2), 251–259 (2016).

Biomedical Optics EXPRESS

53. M. H. Aref, I. H. Aboughaleb, and Y. H. El-Sharkawy, "Tissue characterization utilizing hyperspectral imaging for liver thermal ablation," Photodiagn. Photodyn. Ther. **31**, 101899 (2020).
54. H. Wackerbarth, U. Kuhlmann, F. Tintchev, *et al.*, "Structural changes of myoglobin in pressure-treated pork meat probed by resonance Raman spectroscopy," Food Chem. **115**(4), 1194–1198 (2009).
55. S. Mosca, C. Conti, N. Stone, *et al.*, "Spatially offset Raman spectroscopy," Nat. Rev. Methods Primers **1**(1), 21 (2021).
56. A. Bossi, S. K. V. Sekar, M. Lacerenza, *et al.*, "Time domain diffuse Raman spectroscopy using single pixel detection," Biomed. Opt. Express **14**(11), 5749 (2023).
57. E. I. Tiktopulo and A. V. Kajava, "Denaturation of type I collagen fibrils is an endothermic process accompanied by a noticeable change in the partial heat capacity," Biochemistry **37**(22), 8147–8152 (1998).
58. T. Theodossiou, G. S. Rapti, V. Hovhannisyan, *et al.*, "Thermally induced irreversible conformational changes in collagen probed by optical second harmonic generation and laser-induced fluorescence," Lasers Med. Sci. **17**(1), 34–41 (2002).
59. H. C. Bertram, Z. Wu, F. van den Berg, *et al.*, "NMR relaxometry and differential scanning calorimetry during meat cooking," Meat Sci. **74**(4), 684–689 (2006).
60. X. L. Xu, M. Y. Han, Y. Fei, *et al.*, "Raman spectroscopic study of heat-induced gelation of pork myofibrillar proteins and its relationship with textural characteristic," Meat Sci. **87**(3), 159–164 (2011).
61. L. Zhang, K. Zhang, H. Yang, *et al.*, "Characterization of lard from different adipose tissues: Physicochemical properties, thermodynamics characteristics and crystallization behaviors," J. Food Compos. Anal. **115**, 105021 (2023).
62. Z. Qin, S. K. Balasubramanian, W. F. Wolkers, *et al.*, "Correlated parameter fit of arrhenius model for thermal denaturation of proteins and cells," Ann. Biomed. Eng. **42**(12), 2392–2404 (2014).
63. A. Bossi, L. Bianchi, P. Saccomandi, *et al.*, "Optical signatures of thermal damage on ex-vivo brain, lung and heart tissues using time-domain diffuse optical spectroscopy: data," Zenodo, 2024, https://doi.org/10.5281/zenodo.10685455